IOP Conference Series: Materials Science and Engineering

Study of thermoelectric magnetohydrodynamic convection on solute redistribution during laser additive manufacturing

View the article online for updates and enhancements.

Study of thermoelectric magnetohydrodynamic convection on solute redistribution during laser additive manufacturing

A Kao[1], T Gan[1], C Tonry[1], I Krastins[1,2] and K Pericleous[1]

[1] Centre for Numerical Modelling and Process Analysis, University of Greenwich, Old Royal Naval College, Park Row, London, SE109LS, United Kingdom
[2] Institute of Physics, University of Latvia, Miera iela 32, Salaspils, LV-2169, Latvia

E-mail: a.kao@gre.ac.uk

Abstract. Melt pools formed in laser additive manufacturing (AM) are subject to large thermal gradients, resulting in the formation of thermoelectric currents due to the Seebeck effect. When in the presence of an external magnetic field, a Lorentz force is formed which drives fluid flow in the melt pool. This Thermoelectric Magnetohydrodynamics (TEMHD) phenomenon, can have a significant impact on the melt pool morphology and can alter the microstructural evolution of the solidification process. By coupling steady-state mesoscopic melt pool calculations to a microscopic solidification model, predictions of the resulting microstructure for multiple deposited layers have been obtained. The results indicate that the magnetic field can have a transformative effect on the microstructure and solute redistribution. This study highlights the theoretical potential for using magnetic fields as an additional control system to tailor AM microstructures.

1. Introduction

Additive Manufacturing (AM) is the process of creating complicated 3d objects by joining materials together, typically in a layer-by-layer approach. For the AM processing of metals, a high energy source, such as a laser, is used to melt metallic powder layers successively onto each other. This allows them to join as they solidify. A common AM process is selective laser melting (SLM) [1], which successively melts a thin layer of powder on the print bed. These techniques create a liquid melt pool that travels with the energy source and solidifies in its wake. From a modelling point of view, laser AM can be considered to be a fast welding process. In the melt pool, flow, heat transfer and phase change need to be considered. Consequently, heat loss by radiation [2] and evaporation [3], Marangoni convection [4], spattering [5] and denudation [6] need to be included along with other complex physics. As the melt pool solidifies a microstructure is formed; this is then modified or remelted as the scan is repeated for other layers. This repeated remelting of layers leads to a number of defects that affect the integrity of components. This paper explores a novel control mechanism that has the potential to eliminate some of these defects.

There are two frequently used methods for modelling the microstructure of AM. The Phase Field method (PF) [7-8] can capture the dendritic scale but requires a very fine computational mesh and so only small sections can be modelled. The second is the Cellular Automata method (CA), which is generally used to predict the grain scale and can capture larger sections of the build [9-11].

AM is becoming widespread in industry with diverse applications from biomedical implants [12], energy [13] to aeronautical engine parts [14]. Process related defects [15] can be detrimental to the structural integrity of the final components. They include the formation of pores [16], cracks [17] and

large columnar grains [1]. Additional control mechanisms are therefore desirable to suppress these defects. One relatively unexplored technique is the use of external magnetic fields to exploit the Thermoelectric Magnetohydrodynamic (TEMHD) phenomenon.

Thermoelectric (TE) currents are an inherent part of many solidification processes as they are generated by the combination of large thermal gradients and changes in the Seebeck coefficient. When a magnetic field is applied, these TE currents interact and generate a Lorentz force that drives flow, transporting heat and mass. Significant changes to the solidification process due to TEMHD have been observed experimentally and predicted theoretically [18-22]. The solidification conditions of AM mean that there are high thermal gradients and moderate solidification velocities compared to high undercooled growth and so TEMHD effects should be quite significant. To the authors' knowledge there is a lack of systematic investigation into the effects of TEMHD in AM. Sparse information includes a recently published experimental paper [23], which demonstrates that a 0.12 T magnetic field can lead to beneficial effects on the printed material. There have been a greater number of papers concerning welding. Chen *et al*. [24] conducted welding experiments in a 0.415 T static magnetic field, showing a reduction in width within the transitional region in the microstructure. Another study [25] showed that with a 0.3 T magnetic field the "humping" welding defect could be supressed.

Though the research may currently be sparse it has demonstrated the potential benefits of the application of a magnetic field to AM. The effect of magnetic field direction has been studied more systematically in a recently published paper by the authors [26]. This contribution studies in greater detail how redistribution of solute in the melt pool changes the distribution in the final solidified structure, as a direct consequence of TEMHD-dominated flow modifying the melt pool hydrodynamics by the introduction of the magnetic field.

2. Methodology

The governing equations for each of the physical phenomena present as well as the employed numerical methods are described in this section. A more detailed description is given in [26]. Thermoelectric currents, $\mathbf{J}$, are calculated from a modified Ohm's law [27] given by

$$\mathbf{J} = \sigma(-\nabla\psi + \mathbf{u} \times \mathbf{B} - S\nabla T), \tag{1}$$

where σ, ψ, $\mathbf{u}$, $\mathbf{B}$, S and T are the electrical conductivity, electric potential, fluid velocity, magnetic field strength, Seebeck coefficient and temperature, respectively, and current conservation $\nabla \cdot \mathbf{J} = 0$. The resulting currents interact with the magnetic field generating a Lorentz force, $\mathbf{F} = \mathbf{J} \times \mathbf{B}$. In the melt, this force drives the incompressible fluid flow governed by the Navier-Stokes equations,

$$\rho\left(\frac{\partial\mathbf{u}}{\partial t} + \mathbf{u}\cdot\nabla\mathbf{u}\right) = -\nabla p + \mu\nabla^2\mathbf{u} + \mathbf{J}\times\mathbf{B}, \quad \nabla\cdot\mathbf{u} = 0, \tag{2}$$

where t, ρ, p and μ are time, density, pressure and dynamic viscosity. Heat transport is governed by

$$\frac{\partial T}{\partial t} = \nabla \cdot \alpha\nabla T - \mathbf{u}\cdot\nabla T, \tag{3}$$

where α is the thermal diffusivity. Latent heat of fusion, L_f, is related to temperature through the volumetric enthalpy, H, which is defined as the sum of latent and sensible heats

$$H = fL_f + c_pT, \tag{4}$$

where c_p and f are the specific heat capacity and liquid fraction. The Navier-Stokes equations (2) are solved using the lattice Boltzmann method (LBM) [26, 28, 29] yielding a solution for $\mathbf{u}$. The change of phase and release of latent heat (4) are calculated using an enthalpy-based method. Solutions for the electric potential (1), heat transport (3) and enthalpy (4) use finite difference-based schemes [19, 30].

Equations (1-4) are solved throughout the entire computational domain. Additional boundary conditions represent surface phenomena, including the Marangoni force and heat sources/sinks: the heating laser, heat loss due to evaporation and radiation. The other domain boundaries represent far field conditions, namely the ambient temperature. The domain is electrically insulated. Free slip condition for velocity is set for the top surface of the melt pool.

In this work, microstructure evolution is predicted using a Cellular Automata method (CA) based on the μMatIC code [31-33]. For alloy solidification the concentration of solute in the solid, C_s, and liquid, C_l, are governed by $C_s = kC_l$, where k is the partition coefficient of solute. The concept of solute trapping is introduced to account for both the physical non-equilibrium effect, but also a numerical effect where the computational resolution is much larger than the inter-dendritic spacing. A cell is assumed to be a volume average of both dendrites and the high concentration eutectic structures. The Continuous Growth Model [34] accounts for this by proposing a change to k given by

$$k = \frac{k_e + V/V_D}{1 + V/V_D},$$

(5)

where V is the growth velocity and V_D the 'diffusion' velocity. In this case, $V = u_s$ is the scan velocity and $V_D \approx D_l/L$, where L is some characteristic length typically the interface thickness, but to account for numerical trapping it is much larger, and close to the cell size, giving a value of $k = 0.95$. At the solid-liquid interface, the solid fraction, ϕ_s, rate of change is given by

$$C_l(1 - k)\frac{\partial \phi_s}{\partial t} = -\nabla \cdot (D_e \nabla C_l) + \left[1 - (1 - k)\phi_s\right]\frac{\partial C_l}{\partial t},$$

(6)

where $D_e = (1-\phi_s)D_l + \phi_s D_s$ is the equivalent diffusion coefficient and $T^i = m_l(C_l - C_0)$ is the equilibrium interface temperature with m_l and C_0 being the liquidus slope and reference concentration. The equivalent concentration $C_e = (1-\phi_s)C_l + \phi_s C_s$ enters the solute transport equation given by

$$\frac{\partial C_e}{\partial t} + \mathbf{u} \cdot \nabla C_l = \nabla \cdot (D_e \nabla C_l)$$

(7)

with zero mass flux prescribed at the boundaries.

The multiple layers of the AM process are captured by the microstructure model. A moving mesh approach is employed in such a way that the solidified cells exit at the back of the domain and are reintroduced at the front but lowered by the powder layer depth. A new powder layer is introduced above this. A schematic of the AM process is given in figure 1.

3. Results

The numerical model represents the SLM process of a 70 % efficient 100 W laser, scanning at 0.1 m/s with a beam diameter of 100 μm. In this work two cases are shown, a baseline case with no magnetic field, $|\mathbf{B}| = 0$, and one with a transverse magnetic field. The computational domain is a cuboid with 800 μm in the scan direction, x, 300 μm in the build direction, z, and 600 μm in the magnetic field orientation, y. The mesh comprises 1 μm length cubic cells. Initially the domain is set to the powder phase with a particle size ≈ 10 μm and each particle assigned a random crystallographic orientation. Material properties of Al10Si are used for each the liquid, solid and powder phases [26].

The strong thermal gradients and large variations in interface temperature due to latent heat inherent to AM and welding processes can lead to substantial thermoelectric currents [25]. Electric current

Figure 1. Schematic of the AM process, highlighting the TE current circulation and the moving mesh.

flows downstream in $+x$ from the laser spot to the front of the melt pool then circulates through the solid/powder before re-entering in $+z$ upstream of the melt pool. For clarity upstream is defined as the
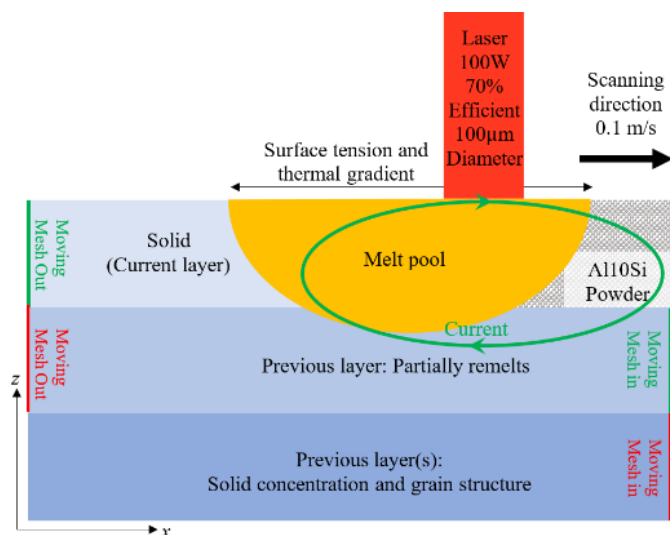
region where the laser has passed and is solidifying and downstream as the melting region at the front of the melt pool. In general, the current in $+y$ is weak compared to the other two components. The structure of these currents is shown in figure 1. When a transverse magnetic field is applied, the Lorentz force has two components, the first is a force in $-z$, downward from the surface of the melt pool and the second is in $+x$ toward the front of the melt pool.

With $|\mathbf{B}| = 0$, fluid flow is governed by Marangoni flow with fluid flowing radially from the laser spot, circulating down the sides of the melt pool and back up to the laser spot. However, for the magnetic field orientation considered, the Lorentz force acts against the returning flow along the centre and if the Lorentz force is dominant it can reverse flow in this region. The force acting in $+x$, stretches the upstream vortex and suppresses the downstream vortex until a single vortex encompasses the melt pool in the x-z plane. In the x-z plane fluid flows down the centre of the melt pool and up the sides.

In the magnetic field case, the melt pool shape is significantly altered compared to the $|\mathbf{B}| = 0$ case. TEMHD introduces a keyhole-like mechanism where hot fluid from the laser spot flows toward the front of the melt pool and downward, deepening the melt pool. However, not only does the change in fluid flow modify heat transfer but it also has a significant effect on solute transport. Schematics of the contrasting behaviour between typical Marangoni flow with no magnetic field and this TEMHD dominated case are given in figures 2 and 3 for no magnetic field and magnetic field respectively.

Using the mesoscopic thermal and velocity profiles as inputs into the microscopic model, a one-way coupling allows for qualitative predictions of solute redistribution. Figure 2 shows cross sections and the grain structures for the $|\mathbf{B}| = 0$ case. The grain structures clearly show that the grains preferentially follow the thermal gradient. Inspecting the dendritic structure, the results indicate that these grains have orientations that align with the thermal gradient. From a thermodynamic perspective the thermal gradient, which also represents the direction of heat flux will favour those with orientations aligned. Therefore, while the powder particles are each assigned random orientations, an initial competition occurs on a short length scale with favourable orientations winning and going to form long needle-like dendrites due to the small primary spacing. However, as the thermal gradient is varying spatially and changes relatively per layer, a secondary competition occurs with larger grains competing, giving rise to very long dendrites from epitaxial growth.

Another consistent feature observed between the numerical model and experimental observations is the formation of a low concentration melt pool boundary, indicated by the white bands in the figures. These form at the very initial stages of solidification on the sides and bottom of the melt pool. With a relatively homogeneous melt pool, solidification initiates without a solute boundary layer and partitioning allows more solute to be ejected, hence a lower concentration in the solid. At the back of the melt pool the solute boundary layer will already have formed and so this low concentration melt pool boundary region forms a shape analogous to the outer surface horizontal cylindrical segment.

At the front of the melt pool melting of the powder doesn't have much effect on the solute distribution. Powders are formed through atomisation processes with finer microstructures than AM and so at the length scales considered here, the powder can be assumed to be homogeneous and of bulk composition. However, when melting a previous layer, solute variations are released back into the melt, an effect that can be seen at the front of the melt pool in the x-z cross section. These variations are captured by the downstream fluid circulation and they are pushed forward allowing time for remixing. However, upstream of the melt pool the fluid circulation passing down the back wall, where the solute boundary is persistent, transports solute back into the melt pool. This can be seen by the plume of solute ejected back into the melt in figure 2(d). However, Marangoni flow also circulates in the y-z plane along the side walls bringing high concentration solute to the bottom centre of the melt pool. This build-up of solute at the base of the melt pool gets captured into the solid forming a thin and long high concentration region along the centre line. This can be seen in the x-z plane just above the low concentration melt pool boundary and also in the y-z plane in the centre. This effect is generally not captured in the x-z plane of experimental results, however we believe this may be simply a case of the difficulty of sectioning perfectly along the centre of the scan axis and also that other investigators may not be looking for this feature. This solute region is around 10-20 microns wide and so any angled section would only appear

as a small region of high concentration. However, experimental sections in the *y-z* plane do consistently show that there is a higher concentration region at the base next to the melt boundary. A good example of this can be seen in the work of Singh *et al.* [35]. For sections in this plane, a small angle deviation will still capture this feature, an analogy is to consider the sectioning of a very long cylinder horizontally vs vertically. By offsetting the *x-z* plane by 20 microns from the centre axis, this solute enriched region vanishes while all the other key microstructure features are still clearly visible. This focused high concentration region is also captured by the upstream Marangoni flow circulation pushing the solute to the top of the melt pool and back. This gives a small increase in the concentration along the centre of the solidified region. However, this effect is somewhat subtle as due to the relatively long time the plume has to circulate through the melt pool, considerable mixing occurs and so the concentration approaching the interface is only slightly elevated.

With the application of the magnetic field the hydrodynamics and melt pool morphology are drastically changed, which consequently has a significant effect on solute redistribution and the microstructure. Figure 3 shows the concentration and grain structure for the case with an applied magnetic field. The grain growth follows the modified thermal gradient, and with a much deeper melt pool the grains become more tilted into the scan direction. There are still epitaxial grains along the centre of the melt pool and they are larger compared to the $|\mathbf{B}| = 0$ case in the *x-z* plane, however, they occupy a smaller transverse *y-z* section. As hot fluid is pushed to the bottom of the melt pool and circulates back up the side walls it cools allowing the side grains to overgrow those from the bottom. This can be seen by the longer side grains in figure 3(a) compared to those in figure 2(a).

Due to the modified hydrodynamics, solute transport is also quite different to the B=0 case. At the front of the melt pool remelting of previous layers brings solute back into the liquid and is swept down into the melt pool and towards the sidewalls. The solute then remixes in the melt pool without a noticeable effect on solidification. However, where solidification begins on the side walls, flow is now going up, transporting high solute concentration to the top sides of the melt pool before circulating back down the centre. Consequently, these high solute regions are captured into the solidification structure near the top of the melt pool, appearing as dark bands in the *x-y* cross section that looks down on the melt pool. The high concentration region at the bottom centre of the melt pool is no longer present due to flow up the side walls transporting concentration from this region away. Redistribution of this high concentration region away from the melt pool boundary may have beneficial effect on the mechanical properties. Experimental studies have shown that the melt pool boundary is a likely site of failure [1], but by reducing the discontinuity in composition, hence material properties this could be mitigated.

In both cases shown here, the laser scans in the same place with each layer. In practice, building macroscopic components will utilise more complex scanning strategies such as hatching, where neighbouring passes of the layers will interact from the sides. Changes to thermal diffusivity and electrical conductivity as the sides are now solid rather than powder, may modify the current density and consequently TEMHD. This may impact the melt pool dynamics, but also remelting and the subsequent regrowth from neighbouring passes may introduce additional microstructure growth features not captured by this idealised scanning strategy.

4. Conclusions

Melt pool dynamics and morphology were predicted using a mesoscopic enthalpy-based method for a Marangoni dominated flow with no magnetic field and a TEMHD dominated flow from a transverse magnetic field. One-way coupling of the thermal and velocity profiles to a microstructural model allowed for predictions of the resulting grain and dendritic structures. Without a magnetic field, features typical of AM processing were well captured and mechanisms of observed solute distribution in the solid were explained. With the application of the transverse magnetic field, changes in melt pool dynamics led to a keyhole-like effect creating a deep melt pool. The TEMHD flow significantly modified the solute distribution with high concentration regions swept to the top of the current layer. The effects of epitaxial growth were analysed over multiple layers in both cases demonstrating the potential of the model used. However, this is an idealised case where scanning occurs in the same

location with each pass, further investigation is necessary to understand how scanning strategy combined with magnetic field strategy can be used to tailor the microstructure in a favourable way. Two- way coupling may also reveal more complex interactions between solute redistribution and phase change.
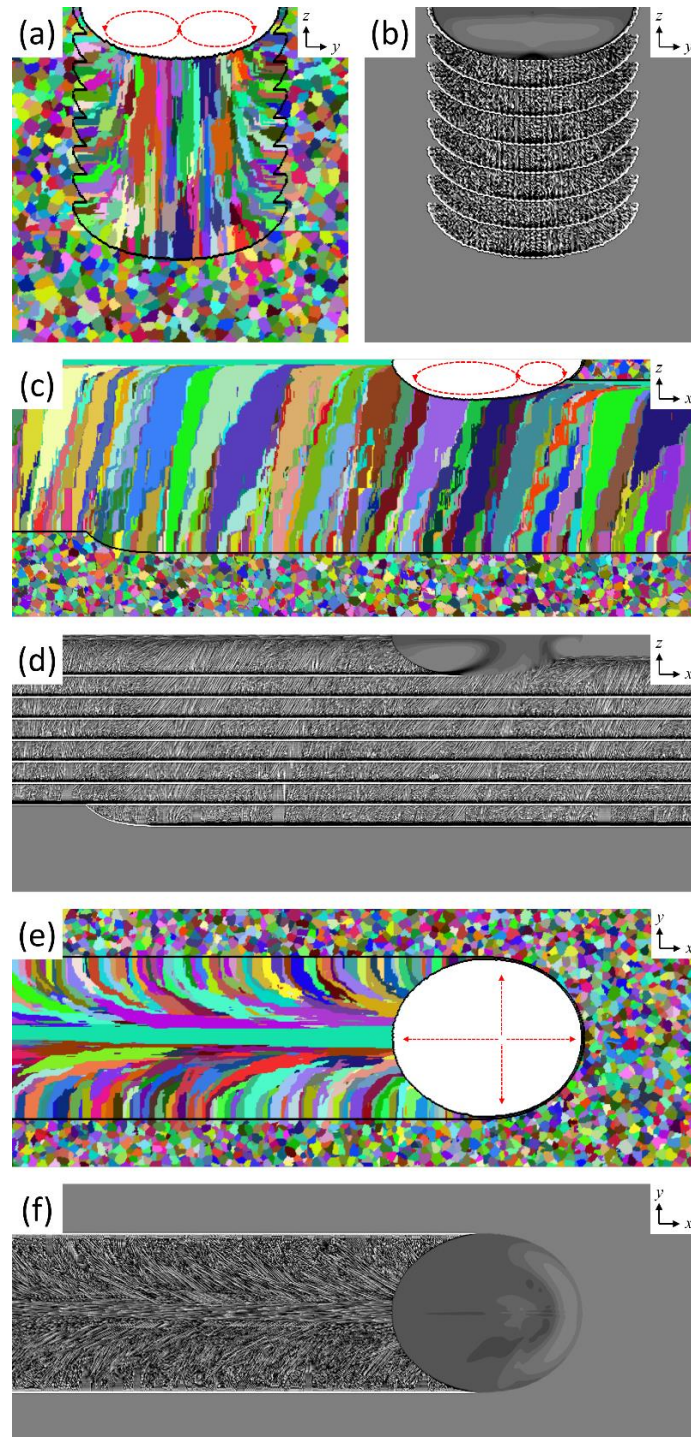

Figure 2. No magnetic field grain structures (a,c,e) and solute concentrations (b,d,f), with darker regions solute enriched, in the *x-z* plane (a,b), the *y-z* plane (c,d) and the *x-y* plane (e,f). Red arrows are schematics of fluid flow. Black lines in (a,c,e) are boundaries between liquid, solid and powder.
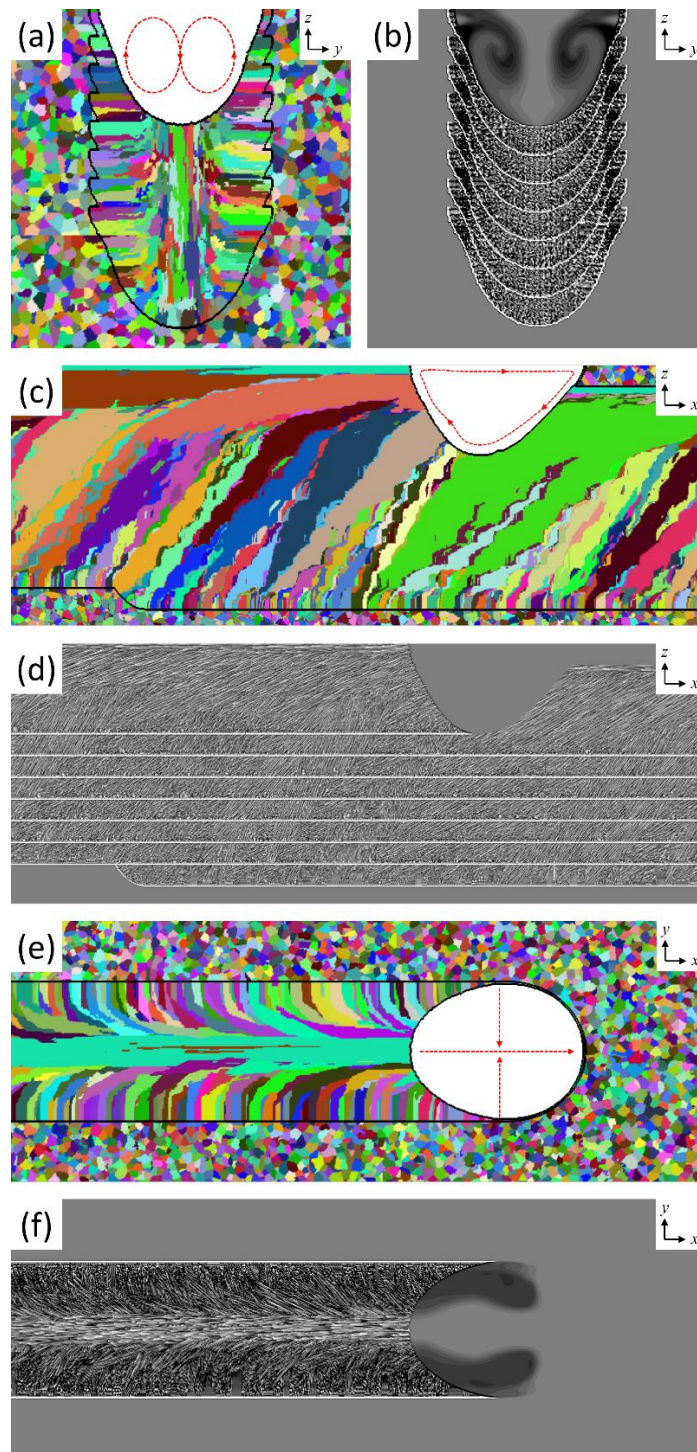
Figure 3. Magnetic field grain structures (a,c,e) and solute concentrations (b,d,f), with darker regions solute enriched, in the *x-z* plane (a,b), the *y-z* plane (c,d) and the *x-y* plane (e,f). Red arrows are schematics of fluid flow. Black lines in (a,c,e) are boundaries between liquid, solid and powder.

References

[1]   Shifeng W, Shuai L, Qingsong W, Yan C, Sheng Z and Yusheng S 2014 *J. Mater. Process. Technol.* **214** 2660–7

[2]   Gusarov A, Yadroitsev I, Bertrand P and Smurov I 2009 *J. Heat Transfer* **131** 072101

[3]   Geiger M, Leitz K H, Koch H and Otto A 2009 *Prod. Eng.* **3** 127–36

[4]   Yuan P and Gu D 2015 *J. Phys. D: Appl. Phys.* **48** 035303

[5]   Khairallah S A, Anderson A T, Rubenchik A and King W E 2016 *Acta Mater.* **108** 36–45

[6]   Matthews M J, Guss G, Khairallah S A, Rubenchik A M, Depond P J and King W E 2016 *Acta Mater.* **114** 33–42

[7]   Wang X and Chou K 2018 *Int. J. Adv. Manuf. Tech.* **100** 2147–62

[8]   Radhakrishnan B, Gorti S B, Turner J A, Acharya R, Sharon J A, Staroselsky A and El-Wardany T 2018 *Metals* **9** 14

[9]   Lian Y, Gan Z, Yu C, Kats D, Liu W K and Wagner G J 2019 *Mat. Des.* **169** 107672

[10] Koepf J A, Gotterbarm M R, Markl M and Körner C 2018 *Acta Mater.* **152** 119–26

[11] Rai A, Markl M and Körner C 2016 *Comput. Mat. Sci.* **124** 37–48

[12] Singh R, Lee P D, Dashwood R J and Lindley T C 2010. *Mater. Technol.* **25** 127–36

[13] Ibrahim K A, Wu B and Brandon N P 2016 *Mat. Des.* **106** 51–9

[14] Murr L E 2016 *J. Mat. Sci. Tech.* **32** 987–95

[15] Zhang B, Li Y and Bai Q 2017 *Chinese J. Mech. Eng.* **30** 515–27

[16] Leung C L A, Marussi S, Atwood R C, Towrie M, Withers P J, Lee P D 2018 *Nat. Comm.* **9** 1355

[17] Li R, Shi Y, Wang Z, Wang L, Liu J and Jiang W 2010 *Appl. Surf. Sci.* **256** 4350–6

[18] Fautrelle Y, Wang J, Salloum-Abou-Jaoude G, Abou-Khalil L, Reinhart G, Li X, Ren Z M and Nguyen-Thi H 2018 *JOM* **70** 764–71

[19] Kao A, Cai B, Lee P and Pericleous K 2017 *J. Cryst. Growth* **457** 270–4

[20] Kaldre I, Fautrelle Y, Etay J, Bojarevics A and Buligins L 2013 *J. Alloys Compd.* **571** 50–55

[21] Gao J, Han M, Kao A, Pericleous K, Alexandrov D V and Galenko P K 2016 *Acta Mater.* **103** 184–91

[22] Kao A, Gao J and Pericleous K 2018 *Philos. Trans. Royal Soc. A* **376** 20170206

[23] Du D, Haley J C, Dong A, Fautrelle Y, Shu D, Zhu G, Li X, Sun B and Lavernia E J 2019 *Mat. Des.* **181** 107923

[24] Chen J, Wei Y, Zhan X and Pan P 2017 *Int. J. Adv. Manuf. Tech.* **92** 1677–86

[25] Kern M, Berger P and Hugel H 2000 *Weld. J. Res. Suppl.* 72–8

[26] Kao A, Gan T, Tonry C, Krastins I and Pericleous K 2020 *Philos. Trans. Royal Soc. A* In press.

[27] Shercliff J A 1979 *J. Fluid Mech.* **91** 231–51

[28] Kao A, Krastins I, Alexandrakis M, Shevchenko N, Eckert S, Pericleous K 2018 *JOM* **71** 48–58.

[29] Kao A, Shevchenko N, Alexandrakis M, Krastins I, Eckert S and Pericleous K 2019 *Philos. Trans. Royal Soc. A* **377** 20180206

[30] Voller V R, Cross M and Markatos N C 1987 *Int. J. Numer. Methods Eng.* **24** 271–84

[31] Wang W, Lee P and McLean M 2003 *Acta Mater.* **51** 2971–87

[32] Yuan L and Lee P D 2010 *Modell. Simul. Mater. Sci. Eng.* **18** 055008

[33] Yuan L and Lee P D 2012 *Acta Mater.* **60** 4917–26

[34] Aziz M J and Kaplan T 1988 *Acta Metall.* **36** 2335–47

[35] Singh A, Ramakrishnan A and Dinda G 2017 *J. Weld. Join.* **35** 67–73